








ARTICLE

<https://doi.org/10.1038/s41467-019-12460-7>

OPEN

# Anchoring Cu<sub>1</sub> species over nanodiamond-graphene for semi-hydrogenation of acetylene

Fei Huang<sup>1,2,11</sup>, Yuchen Deng<sup>3,11</sup>, Yunlei Chen<sup>4,5,11</sup>, Xiangbin Cai <sup>6,11</sup>, Mi Peng<sup>3</sup>, Zhimin Jia<sup>1,2</sup>, Jinglin Xie<sup>3</sup>, Dequan Xiao <sup>7</sup>, Xiaodong Wen <sup>4,8</sup>, Ning Wang <sup>6</sup>, Zheng Jiang <sup>9,10\*</sup>, Hongyang Liu <sup>1,2\*</sup> & Ding Ma <sup>3\*</sup>

The design of cheap, non-toxic, and earth-abundant transition metal catalysts for selective hydrogenation of alkynes remains a challenge in both industry and academia. Here, we report a new atomically dispersed copper (Cu) catalyst supported on a defective nanodiamond-graphene (ND@G), which exhibits excellent catalytic performance for the selective conversion of acetylene to ethylene, i.e., with high conversion (95%), high selectivity (98%), and good stability (for more than 60 h). The unique structural feature of the Cu atoms anchored over graphene through Cu-C bonds ensures the effective activation of acetylene and easy desorption of ethylene, which is the key for the outstanding activity and selectivity of the catalyst.

<sup>1</sup>Shenyang National Laboratory for Materials Science, Institute of Metal Research, Chinese Academy of Sciences, 110016 Shenyang, P. R. China. <sup>2</sup>School of Materials Science and Engineering, University of Science and Technology of China, 230026 Hefei, P. R. China. <sup>3</sup>Beijing National Laboratory for Molecular Engineering, College of Chemistry and Molecular Engineering and College of Engineering, BIC-ESAT, Peking University, 100871 Beijing, P. R. China. <sup>4</sup>State Key Laboratory of Coal Conversion, Institute of Coal Chemistry, Chinese Academy of Sciences, 030001 Taiyuan, P. R. China. <sup>5</sup>University of Chinese Academy of Science, No. 19A Yuanquan Road, 100049 Beijing, P. R. China. <sup>6</sup>Department of Physics, Hong Kong University of Science and Technology, Clear Water Bay, Kowloon, Hong Kong SAR, P. R. China. <sup>7</sup>Center for Integrative Materials Discovery, Department of Chemistry and Chemical Engineering, University of New Haven, 300 Boston Post Road, West Haven, CT 06516, United States. <sup>8</sup>National Energy Center for Coal to Clean Fuel, Synfuels China Co., Ltd, Huairou District, 101400 Beijing, P. R. China. <sup>9</sup>Shanghai Institute of Applied Physics, Chinese Academy of Science, 201800 Shanghai, P. R. China. <sup>10</sup>Shanghai Synchrotron Radiation Facility, Zhangjiang Lad, Shanghai Advanced Research Institute, Chinese Academy of Science, 201210 Shanghai, P. R. China. <sup>11</sup>These authors contributed equally: Fei Huang, Yuchen Deng, Yunlei Chen, Xiangbin Cai. \*email: [jiangzheng@sinap.ac.cn](mailto:jiangzheng@sinap.ac.cn); [liuhy@imr.ac.cn](mailto:liuhy@imr.ac.cn); [dma@pku.edu.cn](mailto:dma@pku.edu.cn)

Selectively hydrogenating remnant acetylene in the raw olefin streams to ethylene while avoiding the over-hydrogenation to undesired ethane is a key industrial reaction to manufacture polymer-grade raw materials for the production of polyethylene<sup>1–3</sup>. The most commonly used industrial catalyst for the reaction is based on supported Pd nanoparticles (NPs) modified by Ag additives<sup>4</sup>. Although the Pd-Ag catalyst prevents the usage of toxic promoters such as lead or sulfur (Lindlar catalyst)<sup>5</sup>, the extremely high cost of Pd leaves ample room for improving the cost-effectiveness in catalyst design. In an effort to develop environment-friendly and cost-effective catalysts, various approaches have been pursued, including (i) reducing the amount of noble metals by “site-isolation” strategy or engineering a minimal ensemble<sup>6–11</sup> and (ii) developing non-noble metals/metal oxides catalysts<sup>12–18</sup>.

The key to the first strategy is to prepare atomically dispersed metal catalysts, a burgeoning class of catalytic materials, in which isolated metal atoms were anchored on the solid supports<sup>7,19–23</sup>. Owing to their unique structural and electronic features, the atomically dispersed noble metal catalysts not only displayed unrivaled advantages for their maximal atomic utilization and high turnover frequency (TOF) but also strongly promoted the studies related to active site identifications and reaction mechanisms<sup>23–28</sup>. For the second approach, it is highly desired to develop new catalysts using cheap, non-toxic, and earth-abundant transition metals, such as Cu or Fe, to achieve comparable catalytic performance to that of Pd-based catalysts. Indeed, non-noble metal oxides have been investigated extensively for the development of low-cost and high-performance alkyne hydrogenation catalysts, including ceria<sup>12–16</sup>. Owing to limited H<sub>2</sub> activation ability<sup>29</sup>, semihydrogenation of alkynes over these oxide catalysts normally required a relatively high-operating temperature. In an elegant work recently, Pardo et al. reported a metal–organic framework-based Fe(III)-O catalyst<sup>18</sup>. This single-site cationic species was active for acetylene hydrogenation at up to 150 °C, which is an important advance in non-noble metal catalyst for this reaction. Alternatively, earth-abundant metal especially Cu-based catalysts have been developed and evaluated for the reaction, suggesting that Cu, as an inexpensive and non-toxic catalyst, has an activity for acetylene hydrogenation over other aforementioned non-noble metals<sup>30</sup>. Yet, a small quantity of Pd promoter was still a must for achieving satisfactory catalytic performance<sup>31,32</sup>.

Herein we report the fabrication of cheap atomically dispersed Cu catalysts without other noble metals to effectively catalyze selective hydrogenation of acetylene. In the followings, we will first show adequate experimental evidences that isolated Cu atoms were anchored over the surface-defective nanodiamond–graphene (ND@G) support (Cu<sub>1</sub>/ND@G). Second, we will demonstrate that Cu<sub>1</sub>/ND@G possessed remarkable catalytic performance: high conversion (95%), high selectivity (98%), and good stability (for >60 h) for acetylene hydrogenation, compared to the Cu-cluster catalyst supported over the same host (denoted as Cu<sub>n</sub>/ND@G). Finally, by density functional theory (DFT) calculations, we will show that the unique structure of the atomically dispersed Cu catalyst facilitates the activation of acetylene and the desorption of ethylene, which is pivotal for the enhanced activity and selectivity of Cu<sub>1</sub>/ND@G compared to Cu<sub>n</sub>/ND@G.

## Results

### Synthesis and characterization of Cu<sub>1</sub>/ND@G and Cu<sub>n</sub>/ND@G.

We prepared the Cu<sub>1</sub>/ND@G and Cu<sub>n</sub>/ND@G catalysts following the preparation procedure in the “Methods” section. Here we will probe the dispersion states of Cu atoms in these two different catalysts. The substrate ND@G features a thin graphene

shell with abundant defects formed during the annealing of ND. High-resolution transmission electron microscope (HRTEM) images (see Fig. 1a and Supplementary Fig. 1), Raman spectra, and X-ray photoelectron spectroscopic (XPS) measurements (see Supplementary Figs. 3 and 4) revealed the unique defect-rich structure of ND@G. The highly defective few-layer graphene outer-shells served as hosts for anchoring metal atoms. By simply modulating the reduction temperature (see the preparation details in the “Methods” section) of Cu species deposited on graphitic carbon shells, we could change the dispersion state of Cu to prepare two different types of catalysts: atomically dispersed Cu catalyst (denoted as Cu<sub>1</sub>/ND@G) and Cu-cluster catalyst (denoted as Cu<sub>n</sub>/ND@G). Importantly, both of them have identical Cu loading amount (0.25 wt%). From X-ray diffraction (XRD) profiles (see Supplementary Fig. 5), no diffraction associated with bulk Cu was detected on both catalysts, demonstrating that the Cu species were highly dispersed over the substrate surface. Further structural analysis of the catalysts (see Supplementary Table 1) revealed that no obvious differences in chemical structure were found between Cu<sub>1</sub>/ND@G and Cu<sub>n</sub>/ND@G except for the dispersion of Cu species. The aberration-corrected high-angle annular dark-field scanning transmission electron microscopic (HAADF-STEM) images showed that the Cu<sub>1</sub>/ND@G catalyst was consisted of isolated bright spots, indicating the atomically dispersed Cu species on ND@G (Fig. 1c, d). In contrast, for Cu<sub>n</sub>/ND@G, the Cu species was dominated by Cu clusters, together with a small amount of atomically dispersed Cu (see Fig. 1e, f). In good agreement with the results of TEM, Cu dispersion state observed by N<sub>2</sub>O titration (99.8% for Cu<sub>1</sub>/ND@G and 85.2% for Cu<sub>n</sub>/ND@G, see Supplementary Table 1) further confirmed that the two catalysts, sharing the same Cu loading, have different atomic dispersion states.

The X-ray adsorption fine structure (XAFS) measurement was employed to further investigate the distinct structure of Cu species. Clearly, the near-edge feature of Cu<sub>1</sub>/ND@G or Cu<sub>n</sub>/ND@G samples was in between of those of Cu foil and CuO (Fig. 2a), indicating that the Cu species were partially positively charged (Cu<sup>δ+</sup>, 0 < δ < 2). Fourier-transformed *k*<sup>2</sup>-weighted extended X-ray absorption fine structure (EXAFS) in *R* space was performed to elucidate the coordination environments of Cu atoms anchored on ND@G. For Cu<sub>1</sub>/ND@G, the only distinct scattering was observed at 1.5 Å that corresponds to the first coordination shell of Cu-C or Cu-O. This evidences the single atom Cu on ND@G through Cu-C bonding, which is further verified by the appearance of Cu-C peak at 283 eV in C 1s XPS spectrum after Cu was loaded on ND@G (Fig. 3a)<sup>32</sup>. In contrast, for Cu<sub>n</sub>/ND@G, besides the scattering of Cu-C at 1.5 Å, a major peak at 2.2 Å that ascribed to Cu-Cu scattering could be observed, indicating the formation of Cu clusters. A wavelet transformation (WT) of Cu *k*-edge EXAFS oscillations also displayed the dispersion of Cu in both samples visually in both *k* and *R* spaces. Figure 2c, d are the WT contour plots of Cu<sub>1</sub>/ND@G and Cu<sub>n</sub>/ND@G that showed a Cu-C back-scattering contribution near 1.5 Å, indicating that both Cu<sub>1</sub> and Cu<sub>n</sub> were anchored on ND@G through the Cu-C bonding. However, as shown in Fig. 2d, another peak at 2.2 Å in Cu<sub>n</sub>/ND@G, which is associated with the Cu-Cu scattering, further verified the dispersion state of Cu clusters.

XPS was used to study the valence states of Cu in two catalysts (Fig. 3b). For Cu<sub>1</sub>/ND@G, the Cu 2p<sub>3/2</sub> peak appeared at 933.7 eV, situated between Cu<sup>0</sup>/Cu<sup>+</sup> (932.4 eV) and Cu<sup>2+</sup> (934.6 eV)<sup>33,34</sup>, which is consistent with the XANES results (Fig. 2a and Supplementary Fig. 6). The results imply that the Cu species in Cu<sub>1</sub>/ND@G interact strongly with the substrate. Through Cu-C bonds, an elevated chemical valence of single atom Cu species due

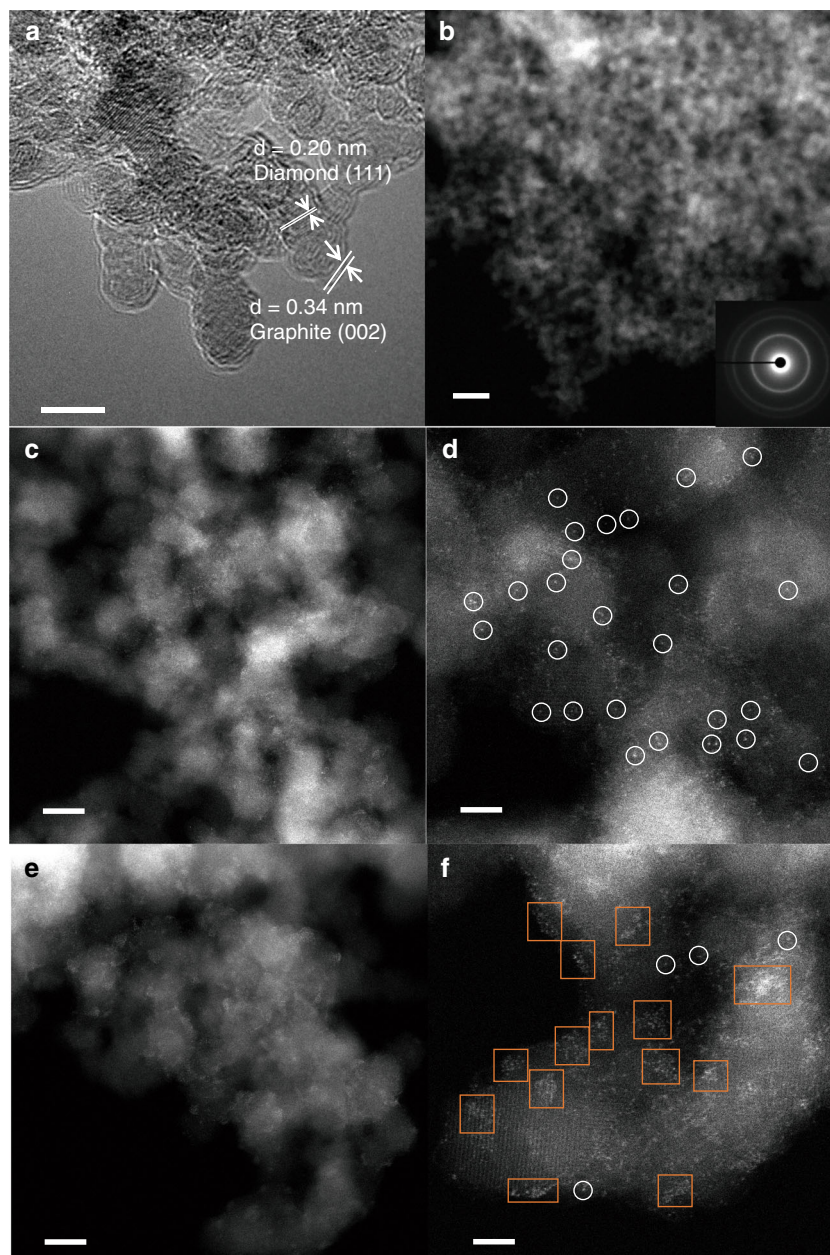


**Fig. 1** TEM characterization of ND@G support and  $\text{Cu}_1/\text{ND@G}$  and  $\text{Cu}_n/\text{ND@G}$  catalysts. **a** HRTEM image of ND@G nanocarbon support. Scale bar, 5 nm. **b** HAADF-STEM image of  $\text{Cu}_1/\text{ND@G}$  at low magnification. Scale bar, 20 nm. **c** HAADF-STEM images of  $\text{Cu}_1/\text{ND@G}$  at low magnification. Scale bar, 5 nm. **d** HAADF-STEM images of  $\text{Cu}_1/\text{ND@G}$  at high magnification. Scale bar, 2 nm. **e** HAADF-STEM images of  $\text{Cu}_n/\text{ND@G}$  at low magnification. Scale bar, 5 nm. **f** HAADF-STEM images of  $\text{Cu}_n/\text{ND@G}$  at high magnification. Scale bar, 2 nm. (The inset attached to **b** is diamond's diffraction rings' image. Atomically dispersed Cu atoms are highlighted by white circles in **d** and Cu clusters are highlighted by orange squares in **f**.)

to charge transferred from Cu atoms to substrate could be observed, which was absent on  $\text{Cu}_n/\text{ND@G}$  due to the similar properties between Cu clusters and bulk Cu.

Quantitative chemical configuration analysis of  $\text{Cu}_1/\text{ND@G}$  and  $\text{Cu}_n/\text{ND@G}$  were carried out through the least-squared EXAFS fitting. The  $R$ -space fitting results are shown in Fig. 2e and Supplementary Fig. 9, and the corresponding structure parameters are listed in Supplementary Table 2. The coordination number of the center Cu atom with surrounding C atoms on  $\text{Cu}_1/\text{ND@G}$  was 3.1, and the mean bond length of Cu-C was 1.94 Å. Based on these results, the proposed local atomic structure of Cu was constructed as that in Fig. 2f. The isolated Cu atom was anchored over the defective sites of graphene through bonding with three C atoms.

**Acetylene hydrogenation performance over  $\text{Cu}_1/\text{ND@G}$  and  $\text{Cu}_n/\text{ND@G}$ .** Selective hydrogenation of acetylene was carried out using  $\text{Cu}_1/\text{ND@G}$  and  $\text{Cu}_n/\text{ND@G}$ , respectively, to gain insight into the impact of the atomic structure and spatial arrangement of Cu over the catalytic performance. The conversion and selectivity as a function of temperature over these two catalysts are shown in Fig. 4a. For aggregated Cu species in  $\text{Cu}_n/\text{ND@G}$ , the conversion was still <20% even at 200 °C. Significantly,  $\text{Cu}_1/\text{ND@G}$  manifested robust catalytic activity and remarkably high selectivity toward ethylene (see Fig. 4a). The conversion of acetylene reached 95% at 200 °C, with ethylene selectivity of 98%. We further compared the intrinsic activity of two catalysts, as shown in Fig. 4b.  $\text{Cu}_1/\text{ND@G}$  showed a high TOF of  $0.0017 \text{ s}^{-1}$  (4.25 times higher than that of  $\text{Cu}_n/\text{ND@G}$ ) and a high ethylene yield

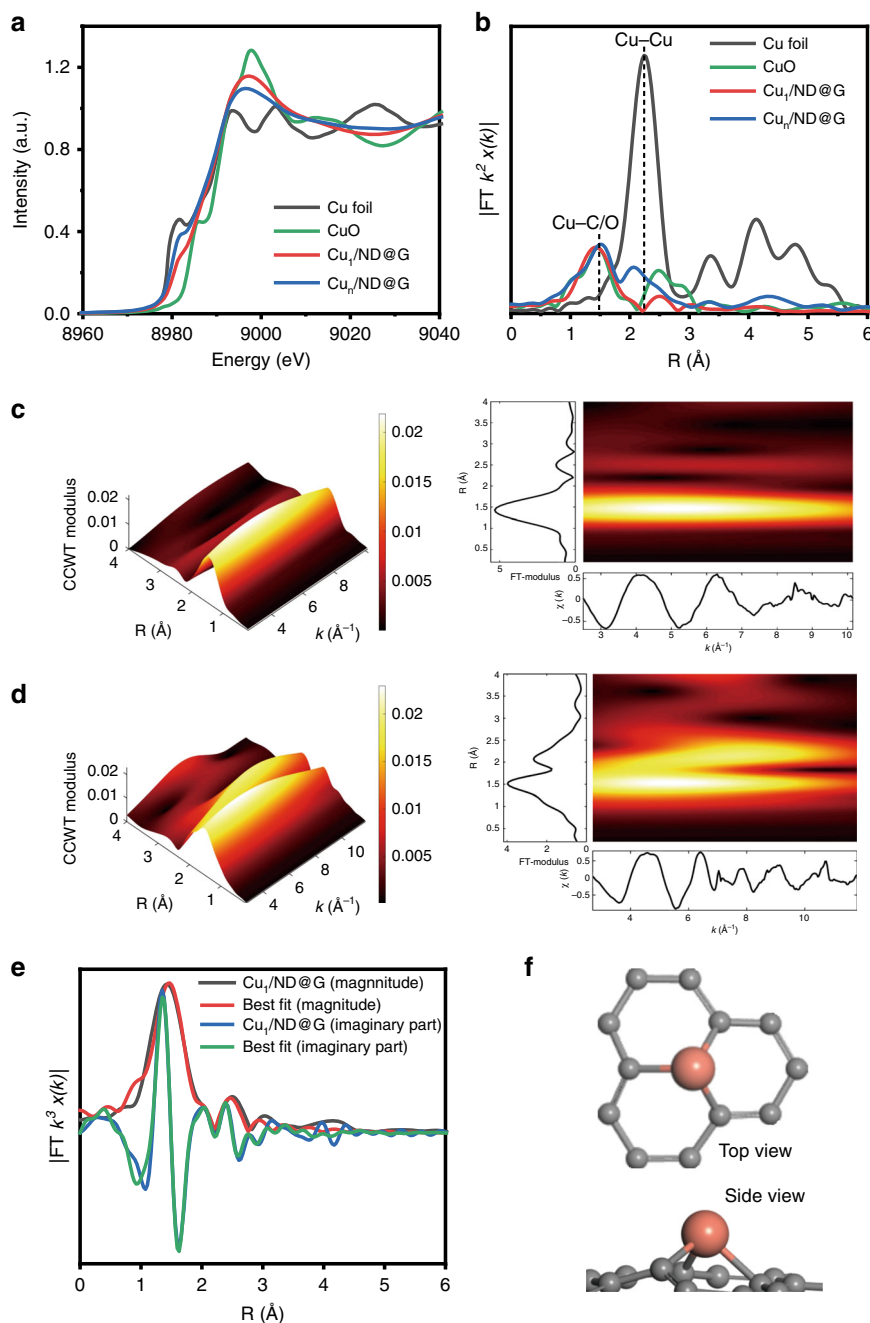


**Fig. 2** Synchrotron XAFS measurements of  $\text{Cu}_1/\text{ND}@G$  and  $\text{Cu}_n/\text{ND}@G$  catalysts. **a** Cu  $k$ -edge XANES profiles for  $\text{Cu}_1/\text{ND}@G$ ,  $\text{Cu}_n/\text{ND}@G$ , Cu foil, and CuO. **b** Cu  $k$ -edge EXAFS spectra in  $R$  space for  $\text{Cu}_1/\text{ND}@G$ ,  $\text{Cu}_n/\text{ND}@G$ , Cu foil, and CuO. **c** WT analysis of  $\text{Cu}_1/\text{ND}@G$ . **d** WT analysis of  $\text{Cu}_n/\text{ND}@G$ . **e** EXAFS fitting curve for  $\text{Cu}_1/\text{ND}@G$ . **f** The optimized Cu-C<sub>3</sub> structure; color code: Cu (orange), C (gray)

of 93.1%, showing competitive advantages over former results [ $<90\%$ ] (see Supplementary Table 3 and Supplementary Fig. 10). Apparent activation energies ( $E_a$ ) of the  $\text{Cu}_1/\text{ND}@G$  and  $\text{Cu}_n/\text{ND}@G$  catalysts were 41.9 and 54.3 kJ/mol, respectively (see Fig. 4c), suggesting the superiority of atomically dispersed Cu catalysts. The stability of  $\text{Cu}_1/\text{ND}@G$  catalyst was found to be excellent. As shown in Fig. 4d, the conversion and selectivity at 200 °C over  $\text{Cu}_1/\text{ND}@G$  remained steady at 95% and 98%, respectively, for at least 60 h under reaction conditions. The atomic structure of the  $\text{Cu}_1/\text{ND}@G$  catalyst was well maintained (see Supplementary Figs. 7–9 and Supplementary Tables 1 and 2) during the stability test. Meanwhile, under the reaction conditions where the conversion is high enough to meet the industrialization

requirement (see Supplementary Fig. 11),  $\text{Cu}_1/\text{ND}@G$  remained stable for at least 30 h.

**DFT calculations.** To better understand the nature of the superior acetylene hydrogenation activity of  $\text{Cu}_1/\text{ND}@G$ , the reaction process was studied by DFT. The details of the computational simulation methods can be found in the “Methods” section.  $\text{Cu}_1$  supported over graphene layer ( $\text{Cu}_1@\text{Gr}$ ) was used to model the  $\text{Cu}_1/\text{ND}@G$  catalyst, while a  $\text{Cu}_{13}$  cluster on ND@G to model the  $\text{Cu}_n/\text{ND}@G$  catalyst. The computational details are summarized in Supplementary Information, including all of the possible binding modes of different adsorbates on the catalytic

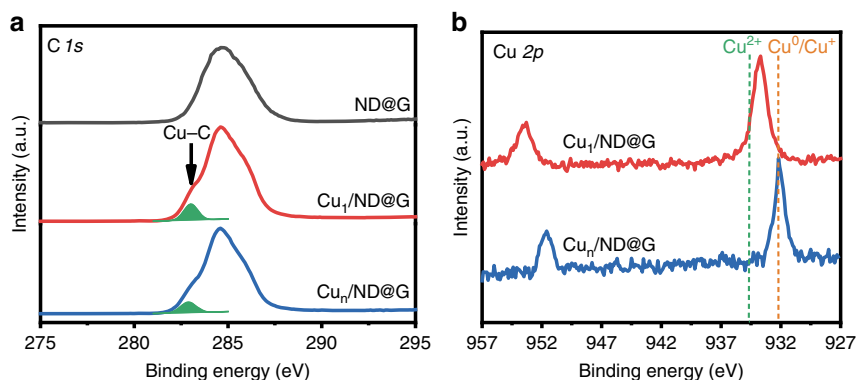


**Fig. 3** XPS measurements of ND@G support and  $\text{Cu}_1/\text{ND@G}$  and  $\text{Cu}_{13}/\text{ND@G}$  catalysts. **a** C 1s XPS of ND@G,  $\text{Cu}_1/\text{ND@G}$ , and  $\text{Cu}_{13}/\text{ND@G}$ . **b** Cu 2p XPS of  $\text{Cu}_1/\text{ND@G}$  and  $\text{Cu}_{13}/\text{ND@G}$

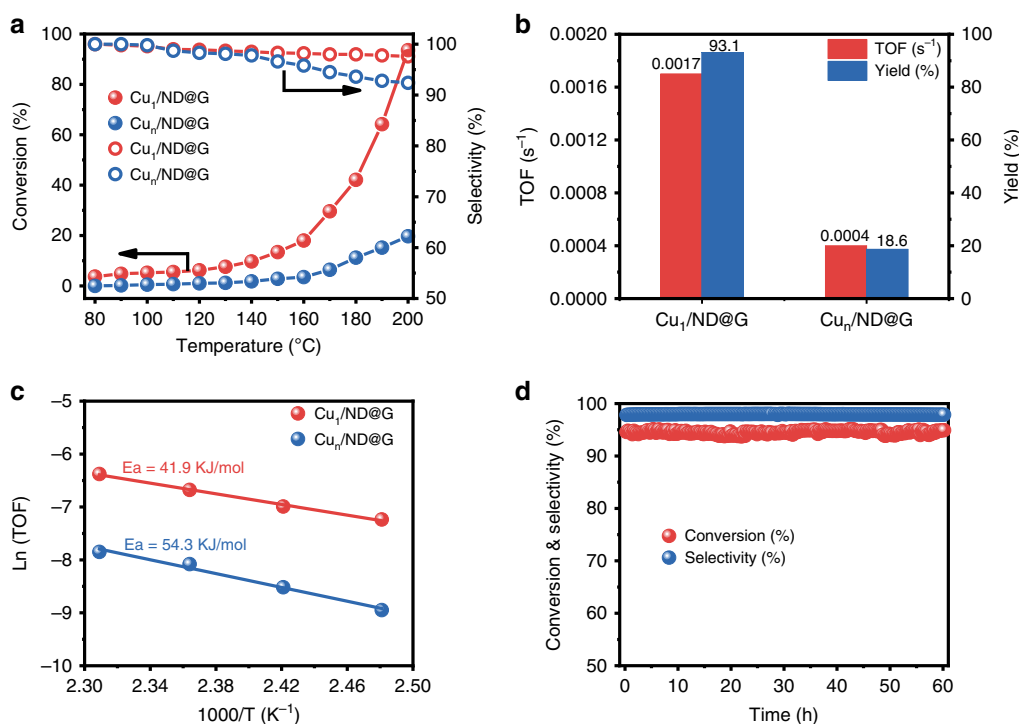


**Fig. 4** Catalytic performance of  $\text{Cu}_1/\text{ND@G}$  and  $\text{Cu}_{13}/\text{ND@G}$ . **a** Conversion and selectivity as a function of temperature for the selective hydrogenation of acetylene over the  $\text{Cu}_1/\text{ND@G}$  and  $\text{Cu}_{13}/\text{ND@G}$  catalysts. **b** TOF values (in the kinetic region) and ethylene yields ( $T = 200\text{ }^\circ\text{C}$ ) of the catalysts. **c** Arrhenius plots of the catalysts. **d** Durability test on  $\text{Cu}_1/\text{ND@G}$  at  $200\text{ }^\circ\text{C}$  for 60 h. (reaction condition: 1%  $\text{C}_2\text{H}_2$ , 10%  $\text{H}_2$ , 20%  $\text{C}_2\text{H}_4$  gas mix balanced with He; GHSV =  $3000\text{ h}^{-1}$ )

surfaces. The energy profiles (including the entropy contribution) for the catalysis of  $\text{Cu}_1/\text{ND@G}$  are shown in Fig. 5. On  $\text{Cu}_1/\text{ND@G}$ , the adsorption energy of acetylene on Cu atoms is  $-1.19\text{ eV}$  (see Supplementary Table 4). Then the molecular hydrogen undergoes dissociative adsorption. This step is exothermic by  $0.36\text{ eV}$  with an energy barrier of  $1.36\text{ eV}$  (from B to C), which is the rate determining step (RDS) for acetylene hydrogenation. On the  $\text{Cu}_{13}$  cluster catalyst, the barrier of RDS is  $1.50\text{ eV}$  (see Supplementary Fig. 14), implying that the cluster catalyst is less active than the  $\text{Cu}_1$  catalyst (see Supplementary Fig. 16). More importantly, the transition-state energy of ethylene hydrogenation on  $\text{Cu}_1/\text{ND@G}$  (TS2,  $1.27\text{ eV}$ ) is above the energy of gas-phase ethylene ( $1.08\text{ eV}$ ), suggesting that ethylene favors desorption over further hydrogenation in the following step. In another word, the high selectivity of acetylene hydrogenation here

is due to the priority of ethylene desorption at the atomically dispersed Cu sites of  $\text{Cu}_1/\text{ND@G}$ . This calculated result is consistent with the observed difference in catalytic performance between  $\text{Cu}_1/\text{ND@G}$  and  $\text{Cu}_{13}/\text{ND@G}$ .

## Discussion

In summary, we synthesized an atomically dispersed  $\text{Cu}_1/\text{ND@G}$  catalyst for acetylene semihydrogenation reaction. It exhibited remarkably outstanding acetylene conversion ( $\sim 95\%$ ), ethylene selectivity ( $\sim 98\%$ ), and stability ( $> 60\text{ h}$ ), exceeding the Cu-cluster catalyst with the same Cu loading. The unique bonding structure and electronic property of Cu atoms on  $\text{Cu}_1/\text{ND@G}$  facilitate the acetylene activation and ethylene desorption, which clearly elucidates the importance of isolated Cu atoms in catalysts for high-

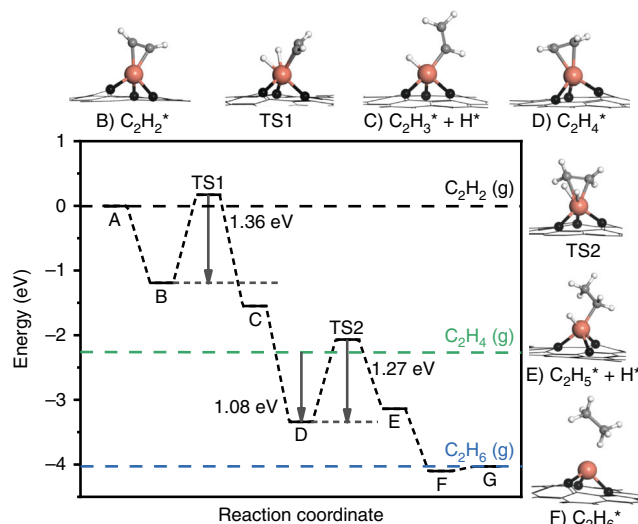


**Fig. 5** Energy profile of acetylene hydrogenation on the  $\text{Cu}_1/\text{ND@G}$  catalyst and the structures of intermediates and transition states. Color code: Cu (orange), C in graphene (black), C in reactant/intermediates/product (gray), and H (white)

performance acetylene semihydrogenation. Our results and conclusions pave the way for rational design of promising non-noble catalysts for hydrogenation processes.

## Methods

**Materials.** ND powders were purchased from Beijing Grish Hitech Co., Ltd, China. Copper (II) nitrate trihydrate ( $\text{Cu}(\text{NO}_3)_2 \cdot 3\text{H}_2\text{O}$ ) was the analytical reagent and purchased from Sinopharm Chemical Reagent Co., Ltd, China. Deionized (DI) water with the specific resistance of 18.25  $\text{M}\Omega \text{ cm}$  was used in all our experiments.

**Preparation of ND@G.** ND@G was prepared by annealing ND powders at  $1100^\circ\text{C}$  (heating rate  $5^\circ\text{C min}^{-1}$ ) for 4 h under flowing Ar gas ( $100 \text{ mL min}^{-1}$ ) and then naturally cooled to room temperature. The as-prepared products were further purified by hydrochloric acid for 24 h and then washed with DI water. Finally, the ND@G nanocarbon support was obtained after drying in vacuum at  $60^\circ\text{C}$  for 24 h.

**Preparation of  $\text{Cu}_1/\text{ND@G}$  and  $\text{Cu}_n/\text{ND@G}$ .** Typically, 200 mg ND@G was dispersed into 30 mL DI water in a 100-mL round-bottom flask, and the mixture was ultrasonically treated for 30 min to obtain a homogeneous suspension. Then the pH value of ND@G support suspension was adjusted to about 11 by dropping 0.25 M  $\text{Na}_2\text{CO}_3$  solution. Afterwards, 4 mL  $\text{Cu}(\text{NO}_3)_2 \cdot 3\text{H}_2\text{O}$  solution (containing  $0.125 \text{ mg mL}^{-1}$  Cu) was introduced into ND@G support suspension dropwise under magnetic stirring at  $100^\circ\text{C}$  in oil bath and then kept stirring for 1 h. At the end, the mixture was naturally cooled to room temperature, collected by filter, washed several times with DI water, and dried in vacuum at  $60^\circ\text{C}$  for 12 h.

The catalysts were reduced in  $\text{H}_2$  (10 vol% in He, flow rate =  $50 \text{ mL min}^{-1}$ ) at  $200^\circ\text{C}$  for 1 h to yield  $\text{Cu}_1/\text{ND@G}$  and at  $600^\circ\text{C}$  for 1 h to obtain  $\text{Cu}_n/\text{ND@G}$ . The catalysts after the 60-h reaction were denoted as  $\text{Cu}_1/\text{ND@G-60h}$  and  $\text{Cu}_n/\text{ND@G-60h}$ , respectively.

**Catalyst characterization methods.** HRTEM images were taken by a FEI Tecnai G2 F20 working at 200 kV. Atomic resolution STEM images were recorded by a JEOL JEM ARM 200CF aberration-corrected cold field-emission scanning transmission electron microscope at 200 kV. XPS were carried out on ESCALAB 250 instrument with Al K $\alpha$  X-rays (1489.6 eV, 150 W, 50.0 eV pass energy) and the C 1s peak at 284.6 eV as internal standard. XRD patterns were collected by using an X-ray diffractometer (Bruker Smart APEX II) using a Cu K $\alpha$  source at a scan rate of  $2^\circ \text{ min}^{-1}$ .  $\text{N}_2$  physisorption were measured at  $-196^\circ\text{C}$  using a Micrometrics ASAP-2020 instrument. The porosity of samples was obtained through Brunauer–Emmett–Teller analysis with the pore volume measured at  $p/p_0 = 0.99$ , and the pore size distribution was analyzed by BJH method from desorption branch. The dispersion of Cu species on catalysts was measured by a surface oxidation–reduction method on a AutoChem II 2920 apparatus. Typically, 200 mg sample was loaded in a quartz U-tube. After pretreatment with He at  $100^\circ\text{C}$  for 30 min, the sample was reduced with 10 vol%  $\text{H}_2$  in Ar at  $200^\circ\text{C}$  for 1 h (flow rate =  $30 \text{ mL min}^{-1}$ ) and cooled to  $90^\circ\text{C}$  in He flow. Then 10 vol%  $\text{N}_2\text{O}$  in He was introduced into the tube and kept for 3 h at  $90^\circ\text{C}$  (flow rate =  $30 \text{ mL min}^{-1}$ ). The sample was purged with He again and cooled to  $50^\circ\text{C}$ , and then the sample was

reduced with 10 vol%  $\text{H}_2$  in Ar (flow rate =  $30 \text{ mL min}^{-1}$ ) from  $50^\circ\text{C}$  to  $450^\circ\text{C}$  with a heating rate of  $10^\circ\text{C min}^{-1}$ . Ultraviolet–Raman spectroscopy was performed on powder samples by using HORIBA LabRam HR Raman spectrometer, and the excitation wavelength was 325 nm with a power of 0.2 mW (exposure 90 s, accumulate 3 times). XAFS measurements were carried out at Shanghai Synchrotron Radiation Facility. Elemental analysis of copper in the solid catalysts was detected by inductively coupled plasma–atomic emission spectrometry (Optima 8300 DV).

**Catalytic performance tests.** The selective hydrogenation activity of the catalysts was conducted in a quartz-bed flow reactor for acetylene hydrogenation with 200 mg catalysts. A gas mixture of 1 vol%  $\text{C}_2\text{H}_2$ , 10 vol%  $\text{H}_2$ , and 20 vol%  $\text{C}_2\text{H}_4$  with He balance (flow rate =  $10 \text{ mL min}^{-1}$ , GHSV =  $3000 \text{ mL g}^{-1} \text{ h}^{-1}$ ) was introduced, followed by ascending temperature testing. Gas chromatograph (GC) injections were done at each temperature after stabilization for 30 min. The reactants and products were analyzed by GC (Agilent 7890 A) equipped with a flame ionization detector and a HP-PLOT AL/S (HP-plot 19091 P-S15, Agilent,  $50 \text{ m} \times 0.32 \text{ mm} \times 8 \mu\text{m}$ ) capillary column with He as the carrier gas.

Acetylene conversion and selectivity to ethylene were calculated as the following:

$$\text{Conversion} = \frac{\text{C}_2\text{H}_2(\text{feed}) - \text{C}_2\text{H}_2}{\text{C}_2\text{H}_2} \times 100\% \quad (1)$$

$$\text{Selectivity} = \left( 1 - \frac{\text{C}_2\text{H}_6 + 2\text{C}_4 \text{ olefin}}{\text{C}_2\text{H}_2(\text{feed}) - \text{C}_2\text{H}_2} \right) \times 100\% \quad (2)$$

**Computational simulations of the catalytic mechanisms by  $\text{Cu}_1/\text{ND@G}$  and  $\text{Cu}_n/\text{ND@G}$ .** All of the catalytic structures were obtained by the geometry optimizations using the plane-wave-based DFT method implemented in the Vienna Ab Initio Simulation Package<sup>35,36</sup>. We describe the electron–ion interaction using the projector augmented wave method<sup>37,38</sup>. The generalized gradient approximation and the Perdew–Burke–Ernzerhof functional<sup>39,40</sup> describes the exchange and correlation energies for all systems. All the calculations take spin polarized into consideration. The plane-wave expansion of the wave functions adopted an energy cutoff of 400 eV. The Monkhorst–Pack  $k$ -point was set to  $3 \times 3 \times 1$  in the reciprocal lattice. The convergence criteria for electronic self-consistent interactions is  $10^{-5}$ . The geometries of bulk and surface were optimized by the conjugate gradient algorithm until the maximum force on any ion was  $<0.03 \text{ eV \AA}^{-1}$ , where all the atoms in the catalyst and adsorbate were fully relaxed. The most stable configurations of the reactant and intermediates on  $\text{Cu}_1/\text{Gr}$  were determined by using the climbing image nudged elastic band method<sup>41</sup>, and vibrational frequencies were analyzed to ensure the transition state with only one imaginary frequency.

## Data availability

The data supporting this article and other findings are available from the corresponding authors upon request. The source data underlying Figs. 2a, b, e, 3a, b, 4a–d, and 5 and Supplementary Figs. 2a, b, 3a–c, 4a–f, 5, 6, 7a, b, 8a, b, 10, 11, 14, 15, and 16 are provided as a Source Data file.

Received: 9 May 2019; Accepted: 11 September 2019;

Published online: 30 September 2019

## References

1. Studt, F. et al. Identification of non-precious metal alloy catalysts for selective hydrogenation of acetylene. *Science* **320**, 1320–1322 (2008).
2. Teschner, D. et al. Understanding palladium hydrogenation catalysts: when the nature of the reactive molecule controls the nature of the catalyst active phase. *Angew. Chem. Int. Ed.* **47**, 9274–9278 (2008).
3. Chan, C. W. A. et al. Interstitial modification of palladium nanoparticles with boron atoms as a green catalyst for selective hydrogenation. *Nat. Commun.* **5**, 5787–5795 (2014).
4. Studt, F. et al. On the role of surface modifications of palladium catalysts in the selective hydrogenation of acetylene. *Angew. Chem. Int. Ed.* **47**, 9299–9302 (2008).
5. López, N. & Vargas-Fuentes, C. Promoters in the hydrogenation of alkynes in mixtures: insights from density functional theory. *Chem. Commun.* **48**, 1379–1391 (2012).
6. Pei, G. X. et al. Ag alloyed Pd single-atom catalysts for efficient selective hydrogenation of acetylene to ethylene in excess ethylene. *ACS Catal.* **5**, 3717–3725 (2015).
7. Vilé, G. et al. A stable single-site palladium catalyst for hydrogenations. *Angew. Chem. Int. Ed.* **54**, 11265–11269 (2015).
8. Huang, F. et al. Atomically dispersed Pd on nanodiamond/graphene hybrid for selective hydrogenation of acetylene. *J. Am. Chem. Soc.* **140**, 13142–13146 (2018).

9. Lin, R. et al. Design of single gold atoms on nitrogen-doped carbon for molecular recognition in alkyne semi-hydrogenation. *Angew. Chem. Int. Ed.* **131**, 514–519 (2019).
10. Wei, S. et al. Direct observation of noble metal nanoparticles transforming to thermally stable single atoms. *Nat. Nanotechnol.* **13**, 856–861 (2018).
11. Huang, X. et al. Enhancing both selectivity and coking-resistance of a single-atom Pd<sub>1</sub>/C<sub>3</sub>N<sub>4</sub> catalyst for acetylene hydrogenation. *Nano Res.* **10**, 1302–1312 (2017).
12. Vilé, G., Bridier, B., Wichert, J. & Pérez-Ramírez, J. Ceria in hydrogenation catalysis: high selectivity in the conversion of alkynes to olefins. *Angew. Chem. Int. Ed.* **51**, 8620–8623 (2012).
13. Vilé, G., Colussi, S., Krumeich, F., Trovarelli, A. & Pérez-Ramírez, J. Opposite face sensitivity of CeO<sub>2</sub> in hydrogenation and oxidation catalysis. *Angew. Chem. Int. Ed.* **53**, 12069–12072 (2014).
14. Werner, K. et al. Toward an understanding of selective alkyne hydrogenation on ceria: on the impact of O vacancies on H<sub>2</sub> interaction with CeO<sub>2</sub>(111). *J. Am. Chem. Soc.* **139**, 17608–17616 (2017).
15. Cao, T. et al. An in situ DRIFTS mechanistic study of CeO<sub>2</sub>-catalyzed acetylene semihydrogenation reaction. *Phys. Chem. Chem. Phys.* **20**, 9659–9670 (2018).
16. Padole, M. C. et al. Adsorption of C<sub>2</sub> gases over CeO<sub>2</sub>-based catalysts: synergism of cationic sites and anionic vacancies. *Phys. Chem. Chem. Phys.* **19**, 14148–14159 (2017).
17. Tejada-Serrano, M. et al. Synthesis of supported planar iron oxide nanoparticles and their chemo- and stereoselectivity for hydrogenation of alkynes. *ACS Catal.* **7**, 3721–3729 (2017).
18. Tejada-Serrano, M. et al. Isolated Fe(III)-O sites catalyze the hydrogenation of acetylene in ethylene flows under front-end industrial conditions. *J. Am. Chem. Soc.* **140**, 8827–8832 (2018).
19. Lin, L. et al. Low-temperature hydrogen production from water and methanol using Pt/α-MoC catalysts. *Nature* **544**, 80–83 (2017).
20. Li, T. et al. Maximizing the number of interfacial sites in single-atom catalysts for the highly selective, solvent-free oxidation of primary alcohol. *Angew. Chem. Int. Ed.* **57**, 7795–7799 (2018).
21. Qiao, B. et al. Single-atom catalysis of CO oxidation using Pt<sub>1</sub>/FeOx. *Nat. Chem.* **3**, 634–641 (2011).
22. Lee, B.-H. et al. Reversible and cooperative photoactivation of single-atom Cu/TiO<sub>2</sub> photocatalysts. *Nat. Mater.* **18**, 620–626 (2019).
23. Derita, L. et al. Structural evolution of atomically dispersed Pt catalysts dictates reactivity. *Nat. Mater.* **18**, 746–751 (2019).
24. Lin, L. et al. A highly CO-tolerant atomically dispersed Pt catalyst for chemoselective hydrogenation. *Nat. Nanotechnol.* **14**, 354–361 (2019).
25. Chen, Z. et al. A heterogeneous single-atom palladium catalyst surpassing homogeneous systems for Suzuki coupling. *Nat. Nanotechnol.* **13**, 702–707 (2018).
26. Qiao, B. et al. Highly efficient catalysis of preferential oxidation of CO in H<sub>2</sub>-rich stream by gold single-atom catalysts. *ACS Catal.* **5**, 6249–6254 (2015).
27. Lin, J. et al. Remarkable performance of Ir<sub>1</sub>/FeOx single-atom catalyst in water gas shift reaction. *J. Am. Chem. Soc.* **135**, 15314–15317 (2013).
28. Cao, L. et al. Atomically dispersed iron hydroxide anchored on Pt for preferential oxidation of CO in H<sub>2</sub>. *Nature* **565**, 631–635 (2019).
29. Riley, C. et al. Design of effective catalysts for selective alkynes hydrogenation by doping of ceria with a single-atom promoter. *J. Am. Chem. Soc.* **140**, 12964–12973 (2018).
30. Kyriakou, G. et al. Isolated metal atom geometries as a strategy for selective heterogeneous hydrogenations. *Science* **335**, 1209–1212 (2012).
31. Pei, G. X. et al. Performance of Cu-alloyed Pd single-atom catalyst for semihydrogenation of acetylene under simulated front-end conditions. *ACS Catal.* **7**, 1491–1500 (2017).
32. Jasson, U. et al. Design of carbide-based nanocomposite thin films by selective alloying. *Surf. Coat. Technol.* **206**, 583–590 (2011).
33. Qu, Y. et al. Direct transformation of bulk copper into copper single sites via emitting and trapping of atoms. *Nat. Catal.* **1**, 781–786 (2018).
34. Gong, J. et al. Synthesis of ethanol via syngas on Cu/SiO<sub>2</sub> catalysts with balanced Cu<sup>0</sup>-Cu<sup>+</sup> sites. *J. Am. Chem. Soc.* **134**, 13922–13925 (2012).
35. Kresse, G. & Furthmüller, J. Efficient iterative schemes for ab initio total-energy calculations using a plane-wave basis set. *Phys. Rev. B* **54**, 11169–11186 (1996).
36. Kresse, G. & Furthmüller, J. Efficiency of ab-initio total energy calculations for metals and semiconductors using a plane-wave basis set. *Comput. Mater. Sci.* **6**, 15–50 (1996).
37. Blöchl, P. E. Projector augmented-wave method. *Phys. Rev. B* **50**, 17953–17979 (1994).
38. Kresse, G. & Joubert, D. From ultrasoft pseudopotentials to the projector augmented-wave method. *Phys. Rev. B* **59**, 1758–1775 (1999).
39. Perdew, J. P., Burke, K. & Ernzerhof, M. Generalized gradient approximation made simple. *Phys. Rev. Lett.* **77**, 3865–3868 (1996).
40. Perdew, J. P. & Wang, Y. Accurate and simple analytic representation of the electron-gas correlation energy. *Phys. Rev. B* **45**, 13244–13249 (1992).
41. Graeme, H., Uberuaga, B. P. & Hannes, J. A climbing image nudged elastic band method for finding saddle points and minimum energy paths. *J. Chem. Phys.* **113**, 9901–9904 (2000).

## Acknowledgements

This work was supported by the Ministry of Science and Technology (2016YFA0204100, 2017YFB0602200), the National Natural Science Foundation of China (91845201, 21573254, 91545110, 21725301, 91645115, 21932002 and 21473003), the Joint Fund of National Natural Science Foundation of China (U1732667), the Youth Innovation Promotion Association, and Chinese Academy of Science (CAS). N.W. hereby acknowledges the funding support from the Research Grants Council of Hong Kong (Project Nos. C6021-14E and 16306818). The XAS experiments were conducted in Shanghai Synchrotron Radiation Facility (SSRF).

## Author contributions

H.L. and D.M. conceived the research. F.H. conducted material synthesis and carried out the catalytic performance test. Y.D., Z.J. and M.P. conducted the X-ray absorption fine structure spectroscopic measurements and analyzed the data. M.P. and J.X. conducted the X-ray photoelectron spectroscopy. Y.C. and X.W. performed the DFT calculations. X.C. and N.W. contributed to the aberration-corrected high-angle annular dark-field scanning transmission electron microscopy. Z.J. performed some of the experiments. The manuscript was primarily written by F.H., Y.D., H.L. and D.M. and revised by D.X. All authors contributed to discussions and manuscript review.

## Competing interests

The authors declare no competing interests.

## Additional information

**Supplementary information** is available for this paper at <https://doi.org/10.1038/s41467-019-12460-7>.

**Correspondence** and requests for materials should be addressed to Z.J., H.L. or D.M.

**Peer review information** *Nature Communications* thanks Antonio Leyva-Pérez and the other anonymous reviewer(s) for their contribution to the peer review of this work. Peer reviewer reports are available.

**Reprints and permission information** is available at <http://www.nature.com/reprints>

**Publisher's note** Springer Nature remains neutral with regard to jurisdictional claims in published maps and institutional affiliations.



**Open Access** This article is licensed under a Creative Commons Attribution 4.0 International License, which permits use, sharing, adaptation, distribution and reproduction in any medium or format, as long as you give appropriate credit to the original author(s) and the source, provide a link to the Creative Commons license, and indicate if changes were made. The images or other third party material in this article are included in the article's Creative Commons license, unless indicated otherwise in a credit line to the material. If material is not included in the article's Creative Commons license and your intended use is not permitted by statutory regulation or exceeds the permitted use, you will need to obtain permission directly from the copyright holder. To view a copy of this license, visit <http://creativecommons.org/licenses/by/4.0/>.

© The Author(s) 2019